Supporting Information

Tai et al. 10.1073/pnas.1716887115

SI Materials and Methods

Optical Generation, Manipulation, and Two-Photon Photopolymerization.
The laser tweezers utilize an ytterbium-doped fiber laser (YLR-10-1064; IPG Photonics; operating at 1,064 nm) and a phase-only spatial light modulator (SLM; P512-1064; Boulder Nonlinear Systems) with 512×512 pixels, each of size 15×15 μm (4, 26). The beam from the laser is first reflected off the SLM, while slightly overfilling the active area of the SLM, and then projected to the back aperture of the objective. The computer-generated holograms are supplied to the SLM by computer software at a rate of 15 Hz, ensuring real-time manipulation. The holographic nature of the trapping system enables generation of arbitrary 3D patterns of laser light with and without phase singularities within the sample (25, 26), thereby greatly enriching the laser-induced initial configurations that then evolve into stabilized 3D solitons.

The two-photon photopolymerization setup is based on a Ti:Sapphire oscillator (Chameleon Ultra II; Coherent) operating at 780 nm with 140-fs pulses at a repetition rate of 80 MHz, directed to an IX-81 Olympus inverted microscope with a computer-guided 3D nanopositioning stage (Nanocube P-611.3SF; Physik Instrumente) and a computer-controlled fast shutter (model LS3Z2, 200 Hz; Uniblitz) (26). The 3D nanopositioning stage is operated by a LabView-based software to follow a predefined path with nanometer precision. The fast shutter is also controlled by the same LabView program to switch on or off the laser writing. The two-photon photopolymerization setup enables photopolymerization of 3D patterns with submicrometer resolution, which allows for fixing the far-field background of our solitons. In this work, after the initial coaxial solitonic structures (Figs. 3*A* and 5*A*) were generated by the laser tweezers, cylindrical-wall exterior to the soliton and pillars passing through the central axis of the soliton were solidified by the means of two-photon photopolymerization. This was enabled by the partially polymerizable nature of chiral LC mixtures within the initial homeotropic state and allowed us to establish the patterned homeotropic boundary conditions in the "outside-of-doughnut-like" exterior of solitons. Fixing the average molecular alignment in this exterior-of-torus region, which coincides with the north-pole preimage of an elementary soliton, fixes the far-field $\mathbf{n}_0$. The laser power used for two-photon photopolymerization was controlled within 20–35 mW and the pixel dwell time was varied within 10–40 ms.

The 3D Nonlinear Optical Imaging. The nonlinear optical imaging of $\mathbf{n(r)}$ within solitons was performed by using a three-photon excitation fluorescence polarizing microscopy (3PEF-PM) set-up built around an IX-81 Olympus inverted microscope (26). Molecules in the partially polymerizable chiral LC mixture were excited via three-photon absorption by using a Ti-Sapphire oscillator (Chameleon Ultra II; Coherent) operating at 870 nm with 140-fs pulses at a repetition rate of 80 MHz (26). The fluorescence signal was epidetected by using a 417/60-nm bandpass filter by a photomultiplier tube (H5784-20; Hamamatsu). An oil-immersion 100× objective with NA = 1.4 was used. Imaging artifacts such as beam defocusing and polarization changes due to the birefringence of the partially polymerizable chiral LC were mitigated by using the LCs, such as AMLC-0010 with the relatively low birefringence ($\Delta n = 0.08$; Table S2), as the nematic host of the mixture for both LC and ferromagnetic host medium of the solitons. The polarization state of the excitation beam was controlled by using a polarizer and a rotatable half-wave retardation plate or a quarter-wave retardation plate. The detection channel utilized no polarizers. The

3PEF-PM intensity scales as $\cos^6\beta$, where β is the angle between $\mathbf{n(r)}$ and the polarization of the excitation beam (4, 26). The 3D 3PEF-PM images for different polarizations of the excitation light were obtained by scanning the excitation beam through the sample volume and recording the fluorescence intensity as a function of scanning coordinates. The images were then post-processed by background subtraction, depth-dependent intensity normalization, and contrast enhancement. For a given linear polarization of the beam, each 3PEF-PM image yielded pre-images of two antipodal points on the equator of $\mathbb{S}^2$ for a vector field, or a preimage of a single point on $\mathbb{S}^2/\mathbb{Z}_2$ for a director field, due to the nonpolar response of molecules in LC to the excitation. For a vector field, the preimages were then assigned to $\mathbf{n}$ or $-\mathbf{n}$ on the basis of response to the external magnetic field and by comparing the experimental preimages to preimages obtained in numerical modeling. Computer simulations of the 3PEF-PM images were based on the $\propto\cos^6\beta$ dependence of the fluorescence image intensity on the molecular director orientation relative to the linear polarization direction of the excitation light.

The 3D nonlinear optical imaging is supplemented by the conventional polarizing optical microscopy (POM) in the transmission mode by using the same multimodal imaging setup built around the IX-81 Olympus inverted microscope and a charge-coupled device camera (Flea; PointGrey). The integration of nonlinear optical imaging modality, POM modality, laser tweezers, and two-photon photopolymerization capabilities in the same multimodal optical setup allows for fully optical generation, control, and nondestructive imaging of the topological solitons. The POM images were computer-simulated based on the Jones matrix approach (4, 25) and by using the birefringence of the AMLC-0010 nematic host (Table S2).

Numerical Modeling. For chiral nematic LCs with helical pitch p, the Frank–Oseen free-energy functional describing the energetic cost of spatial deformations of $\mathbf{n(r)}$ reads

$$
\begin{aligned}
F = \int d^3\mathbf{r}\Big\{ & \frac{K_{11}}{2}(\nabla\cdot\mathbf{n})^2 + \frac{K_{22}}{2}[\mathbf{n}\cdot(\nabla\times\mathbf{n})]^2 \\
& + \frac{K_{33}}{2}[\mathbf{n}\times(\nabla\times\mathbf{n})]^2 + K_{22}q_0\mathbf{n}\cdot(\nabla\times\mathbf{n}) \\
& - K_{24}\{\nabla\cdot[\mathbf{n}(\nabla\cdot\mathbf{n}) + \mathbf{n}\times(\nabla\times\mathbf{n})]\}\Big\},
\end{aligned}
\quad\text{[S1]}
$$

where $q_0 = 2\pi/p$ characterizes the LC chirality and the Frank elastic constants K_{11}, K_{22}, K_{33}, and K_{24} describe the energetic costs of splay, twist, bend, and saddle-splay deformations, respectively. The surface energy is not included by assuming strong boundary conditions on the surfaces, which is consistent with experiments. When an external electric field is applied, additional coupling terms in the free energy need to be included due to the dielectric properties of the LCs, so that Eq. **S1** is supplemented with the corresponding electric field coupling term,

$$
F_{\text{electric}} = -\frac{1}{2}\int d^3\mathbf{r}(\mathbf{E}\cdot\mathbf{D}) = -\frac{1}{2}\int d^3\mathbf{r}\left(\mathbf{E}\cdot\overline{\overline{\varepsilon}}\,\mathbf{E}\right),
\quad\text{[S2]}
$$

where $\mathbf{E}$ is the applied electric field, $\mathbf{D}$ is the electric displacement field in the dielectric LC medium, and $\overline{\overline{\varepsilon}}$ is the dielectric tensor with components $\varepsilon_{ij} = \varepsilon_0(\varepsilon_\perp\delta_{ij} + \Delta\varepsilon n_i n_j)$, where ε_0 is the

vacuum permittivity and dielectric constants and anisotropy of the used materials are provided in Table S2.

For chiral ferromagnetic LC colloids (CFLCCs) with intrinsic helicoidal pitch p and $\mathbf{m}(\mathbf{r}) = \mathbf{M}(\mathbf{r})/|\mathbf{M}(\mathbf{r})|$ unit vector field describing the coupled molecular alignment and magnetization fields, the free energy reads (5–8)

$$F_{CFLCC} = \int d^3\mathbf{r}\left\{\frac{K_{11}}{2}(\nabla \cdot \mathbf{m})^2 \right.$$
$$+ \frac{K_{22}}{2}[\mathbf{m} \cdot (\nabla \times \mathbf{m})]^2 + \frac{K_{33}}{2}[\mathbf{m} \times (\nabla \times \mathbf{m})]^2$$
$$+ K_{22}q_0\mathbf{m} \cdot (\nabla \times \mathbf{m})$$
$$\left. - K_{24}\{\nabla \cdot [\mathbf{m}(\nabla \cdot \mathbf{m}) + \mathbf{m} \times (\nabla \times \mathbf{m})]\}\right\},$$
[S3]

where again $q_0 = 2\pi/p$ characterizes the intrinsic chirality of the CFLCC, $\mathbf{m} = \mathbf{M}/|\mathbf{M}|$ is the magnetization unit vector, and K_{11}, K_{22}, K_{33}, and K_{24} are the Frank elastic constants (5–8). The coupling between the molecular alignment and magnetization fields is considered being infinitely strong, since only weak or no external magnetic fields are applied in this work (8). When external magnetic fields are present, we supplement the free energy of the CFLCC system in Eq. S3 with the coupling term between the magnetic field $\mathbf{H}$ and the magnetization $\mathbf{M}$

$$F_{magnetic} = -\mu_0 \int d^3\mathbf{r}(\mathbf{H} \cdot \mathbf{M}),$$
[S4]

while disregarding the higher-order diamagnetic coupling term. In CFLCCs, the magnetization $\mathbf{M}$ is determined by both the average dipole moment of the ferromagnetic nanoplatelets and the platelet concentration in the nematic LC host. We set in simulations the dipole moment to be 1.2×10^{-17} A·m^2 and the platelet concentration to be 10 μm^{-3}, based on the values used in experiments (5, 6, 8).

For topological solitons to be considered stable in chiral LCs and CFLCCs at various applied fields, the field configurations need to emerge as local or global minima of the free energy given by Eqs. S1–S4, respectively. Numerical modeling of the energy-minimizing $\mathbf{n}(\mathbf{r})$ and $\mathbf{m}(\mathbf{r})$ structures is performed by using a variational-method-based relaxation routine (4, 8, 25, 26). For example, in the case of $\mathbf{n}(\mathbf{r})$, at each iteration of the numerical simulation, $\mathbf{n}(\mathbf{r})$ is updated based on an update formula derived from the Lagrange equation of the system, $n_i^{new} = n_i^{old} - \frac{MSTS}{2}[F]_{n_i}$, where the subscript i denotes spatial coordinates, $[F]_{n_i}$ denotes the functional derivative of F with respect to n_i, and MSTS is the maximum stable time step in the minimization routine, determined by the values of elastic constants and the spacing of the computational grid (25). The steady-state stopping condition is determined by monitoring the change in the spatially averaged functional derivatives over iterations. When this value approaches zero, the system is implied to be in a state corresponding to the energy minimum, and the relaxation routine is terminated.

The Frank elastic constants adopted in the numerical modeling are based on values for the two nematic hosts used in this study (Table S2) (4, 8, 25, 26). The saddle-splay elastic constant K_{24} was assumed to be zero (4, 25). The 3D spatial discretization is performed on large 3D square-periodic grids, the 128 × 128 × 32 and 90 × 90 × 43 grids, and the spatial derivatives are calculated by using finite difference methods with second-order accuracies, allowing us to minimize discretization-related artifacts in modeling of the structures of the solitons. The grid spacing is set to be 1 μm in all mutually orthogonal directions, so that the cell thickness d values are either 32 or 43 μm. Cylindrically patterned boundary conditions are set by enforcing perpendicular alignment on the top and bottom substrates, as well as in the region exterior to the cylindrical wall enclosing the soliton, fixing the far field $\mathbf{n}_0 = (0,0,1)$ or $\mathbf{m}_0 = (0,0,1)$. To help stabilize solitons, a pillar-like region along the central axis can also be fixed to align director or magnetization along the far field, producing "doughnut-like" patterned boundary conditions. Both the analytical ansatz configurations (24) and manipulations of the stabilized configurations of the analytical ansatz are used as initial conditions. To construct a preimage of a point on $\mathbb{S}^2$ within the 3D volume of the static topological solitons, we calculate a scalar field defined as the difference between the solitonic field $\mathbf{n}(\mathbf{r})$ and a unit vector defined by the target point on $\mathbb{S}^2$. The preimage is then visualized with the help of the isosurfaces of a small value in this ensuing scalar field (4, 8). The freely available software KnotPlot (www.knotplot.com) is used for simplifying and visualizing linking of preimages.

Determination and Switching of Hopf Indices of Topological Solitons. The Hopf index Q of a 3D topological soliton, the topological generalization of the Skyrmion winding number in 2D (9), has a geometrical interpretation as the linking number of the preimages. In general, the preimage of a point on $\mathbb{S}^2$ is a collection of closed loops in $\mathbb{R}^3$. Two preimages of any two distinct points on $\mathbb{S}^2$ are linked exactly Q times, where Q is the Hopf index. By choosing the circulation of the preimage of the north pole on $\mathbb{S}^2$ to be along the vectorized far-field $\mathbf{n}_0$ or $\mathbf{M}_0$ through the center of the topological solitons, we consistently define the circulations of all other preimages by smoothly moving away from the north pole and exploring $\mathbb{S}^2$. The linking number of preimages is then defined as half the total number of crossings (9), with the sign of each crossing defined by the convention based on the right-hand rule. Within this procedure, by flattening the right hand, we extend the fingers in the direction along the circulation of one preimage with the palm facing the other. The sign of the crossing is then positive if the circulation of the other preimage and the thumb's direction point toward the same side with respect to the first preimage, and negative otherwise. The values of Q at all applied fields determined via this approach are consistent with the ones obtained via numerical integration (Table S1), as described below. Electric switching of Q of the topological solitons was achieved by applying voltages to transparent indium tin oxide electrodes of glass cells using a function generator (DS345; Stanford Research Systems) with sinusoidal output operated at 1 kHz.

The Hopf index Q is also computed by integrating a topological charge density in either $\mathbb{S}^3$ or $\mathbb{R}^3$ according to Eq. **1** (20–24). By defining $b^i \equiv \epsilon^{ijk}F_{jk}$, one gets $b^i = \epsilon^{ijk}(\partial_j A_k - \partial_k A_j)/2 = \epsilon^{ijk}\partial_j A_k$, and $\mathbf{A}$ can be understood as the vector potential of the vector field $\mathbf{b}$, since $\mathbf{b} = \nabla \times \mathbf{A}$, and Q can be rewritten as $Q = 1/64\pi^2 \int d^3\mathbf{r}\mathbf{b} \cdot \mathbf{A}$. After calculating $\mathbf{b}$ from the unit vector field $\mathbf{n}(\mathbf{r})$, the vector potential $\mathbf{A}$ can be obtained by numerically solving the differential equation $\mathbf{b} = \nabla \times \mathbf{A}$, or constructed by the direct integration of $\mathbf{b}$ (24). The latter method is briefly described as follows. By picking a convenient gauge such that $A_z = 0$, we integrated A_x and A_y from $b_x = -\partial_z A_y$ and $b_y = \partial_z A_x$. The integration constants were then determined by assuring $b_z = \partial_x A_y - \partial_y A_x$. The values reported in (Table S1 are based on the method of a direct integration. Before the numerical integration to obtain the Hopf index, the numerical solitonic field configurations were interpolated on a grid 10 times finer than the original grid, for which the free-energy minimization was performed, which was needed to achieve the numerical precision of Hopf index values presented in Table S1.
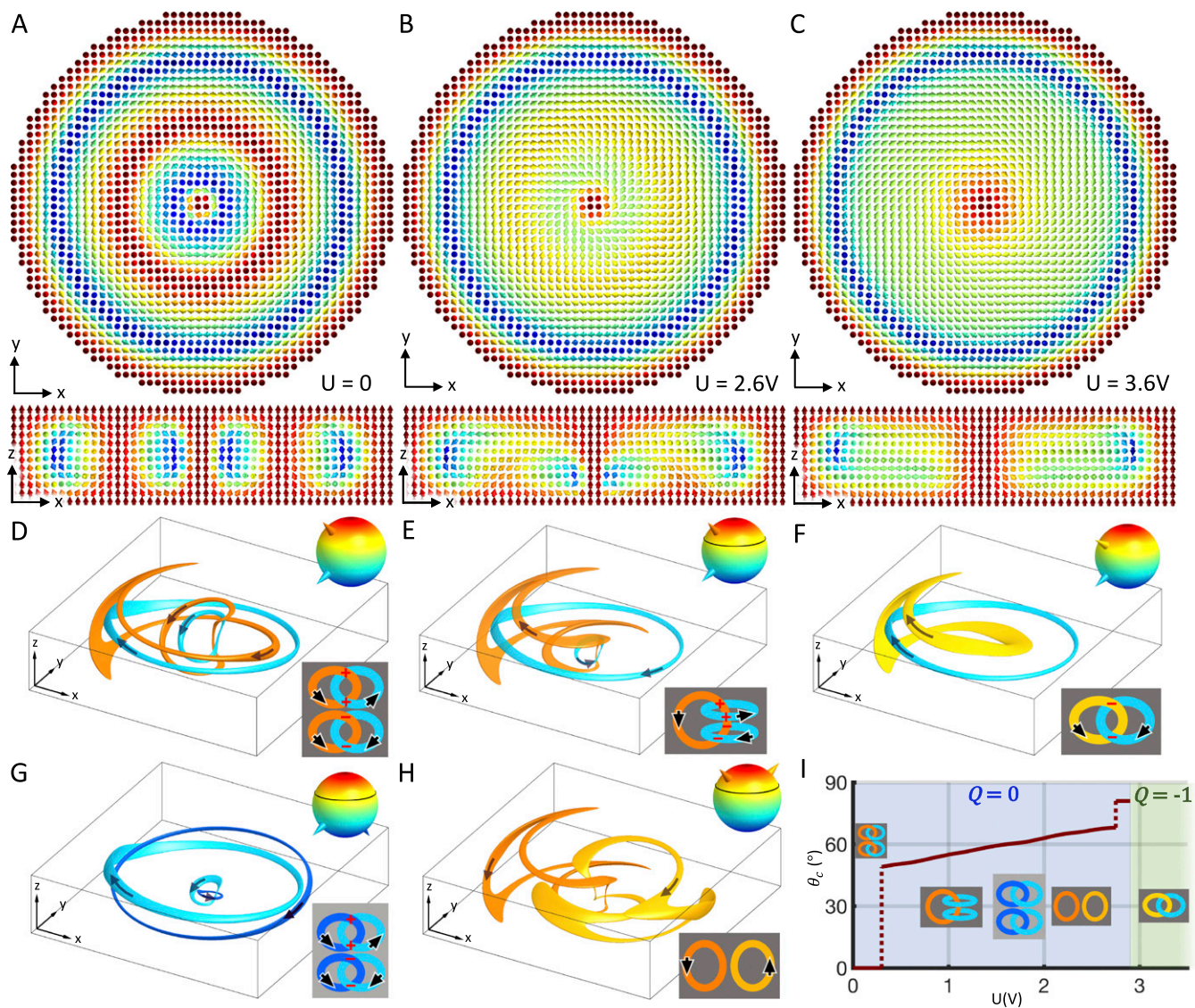
Fig. S1. Electric switching from $Q = 0$ to $Q = -1$ (additional details for Fig. 5). (*A–C*) Computer-simulated cross-sections of the solitons stabilized at different U in the plane orthogonal to $\mathbf{n}_0$ (*Upper*) and in the vertical plane containing $\mathbf{n}_0$ (*Lower*). (*D–H*) The 3D preimages in $\mathbb{R}^3$ of points on $\mathbb{S}^2$ shown as cones in *Upper Right Insets*. (*D* and *F* correspond to the solitons shown in *A* and *C*, respectively, while *E*, *G*, and *H* correspond to *B*). *Lower Right Insets* show the schematics of the linking of preimages, with the signs of the crossings marked in red. Arrows on preimages represent their consistently determined circulations. In *D*, preimages of distinct points on $\mathbb{S}^2$ form a pair of Hopf links with linking numbers +1 and −1, yielding a net linking number 0. In *E*, *G*, and *H*, a preimage can be a single loop (0_1) or a pair of unlinked closed-loops (0_1^2), depending on the location of the corresponding point on $\mathbb{S}^2$, with the subspaces separated by a critical polar angle $\theta_c = 67.5°$. For all combinations of distinct points on $\mathbb{S}^2$, the net linking number is 0. In *F*, a preimage is a single loop and the linking number is −1 for all pairs of distinct preimages. (*I*) Critical polar angle θ_c and Hopf index Q of the soliton vs. U. The regions with $Q = 0$ and $Q = -1$ are shown using different background colors and labeled respectively. Note the abrupt transitions in θ_c at U = 0.3 V and at U = 2.8 V, as well as the discontinuous Q-changing transition from $Q = 0$ to $Q = -1$ at U = 2.9 V. Schematics of preimage linking within each voltage range are shown as *Insets*. Computer simulations were performed for elastic constants of AMLC-0010 and $d/p = 1.35$.
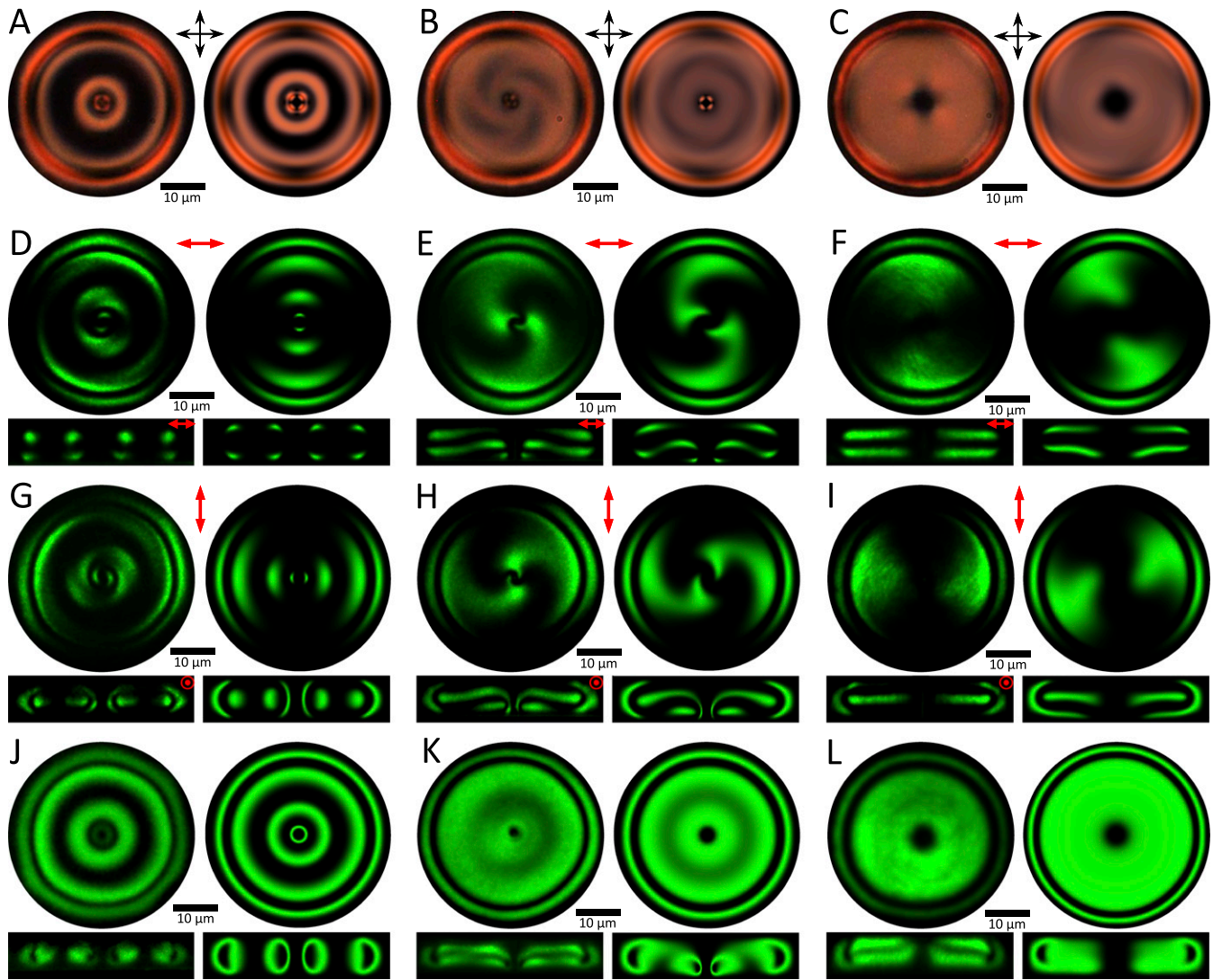
Fig. S2. Comparison of experimental and computer-simulated optical images of solitons shown in Fig. 5. The images in *Left* are obtained experimentally, and those in *Right* are computer-simulated. (*A–C*) Polarizing optical micrographs of solitons corresponding to Fig. 5 *A–C*, respectively. (*D–L*) Cross-sectional non-linear optical images of solitons corresponding to structures in Fig. 5*A* in the case of *D*, *G*, and *J*, to configurations in Fig. 5*B* in the case of *E*, *H*, and *K*, and Fig. 5*C* in the case of *F*, *I*, and *L*. *Upper* images are midplane cross-sections orthogonal to $\mathbf{n}_0$, and *Lower* images are cross-sections parallel to $\mathbf{n}_0$ and passing through the central axes of the solitons. The polarization states of excitation light are linear in *D–I*, as marked in *Upper Right* of the experimental images, and are circular in *J–L*. Note that since the field topologies of the soliton in Figs. 3*C* and 5*C* are similar, the experimental images in *F*, *I*, and *L* are the same as the images shown in Fig. 4 *F–L*. The experiments were performed by using the partially polymerizable mixture based on AMLC-0010 confined in a glass cell with $d/p \sim 1.35$.
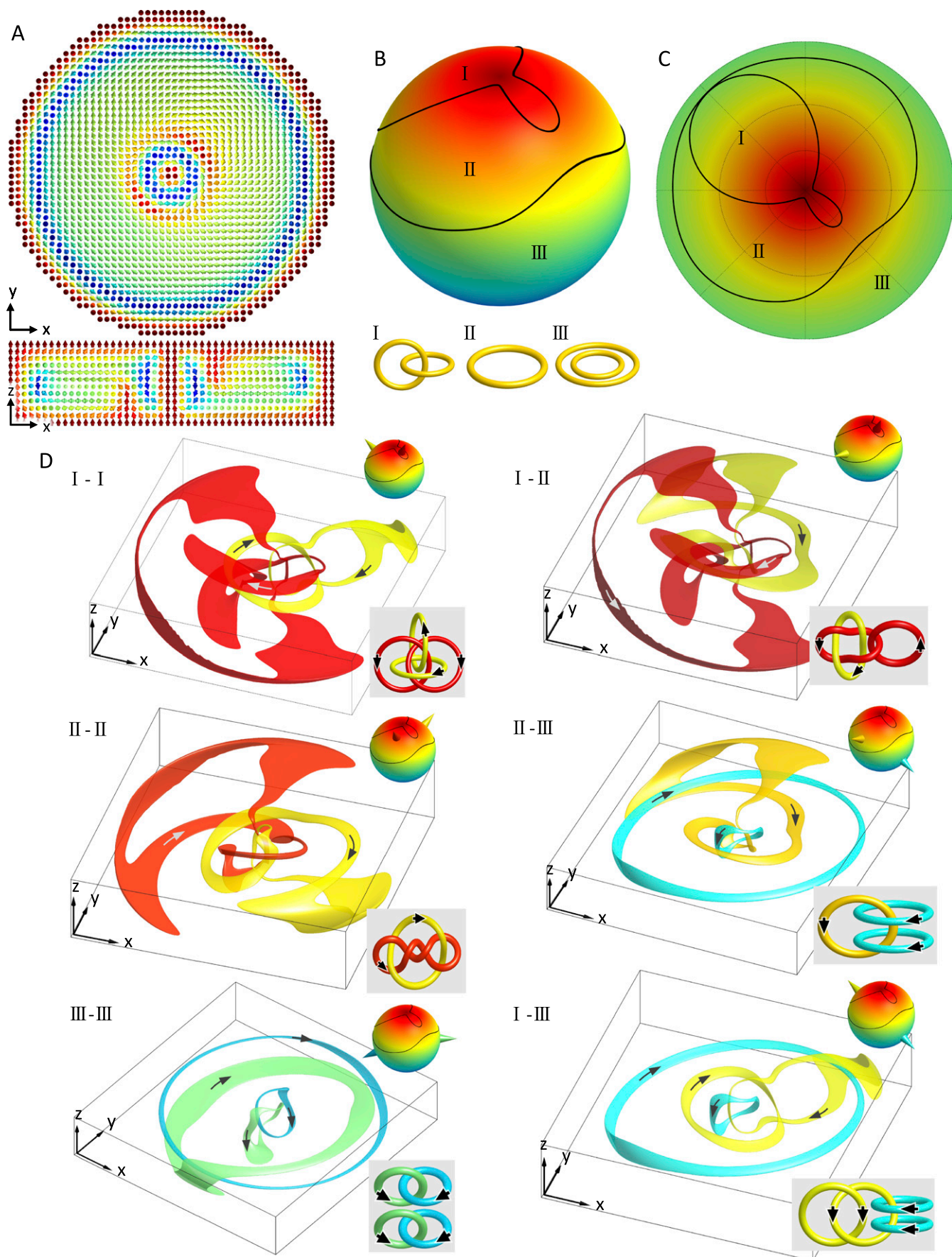
Fig. S3. Preimages of the $Q = -2$ soliton with broken axial symmetry (additional details for Fig. 6). (*A*) Cross-sections of the field configuration of the soliton in the *x–y* plane orthogonal to $\mathbf{n}_0$ (*Upper*) and in the *x–z* plane parallel to $\mathbf{n}_0$ passing through the soliton's center (*Lower*). (*B*) The ground-state manifold $\mathbb{S}^2$ is divided into three subspaces (I, II, and III), with preimages of points in each subspace pictured in *Lower* and the boundaries between subspaces shown by using black lines. (*C*) The stereographic projection of the northern hemisphere of the preimage topology map on $\mathbb{S}^2$. (*D*) Reconstructed 3D preimages of pairs of distinct points with their corresponding subspaces on $\mathbb{S}^2$ (I, II, and III) identified. *Upper Right Insets* show the points on $\mathbb{S}^2$ as cones corresponding to the preimages, and *Lower Right Insets* show the simplified schematics of the link of preimages. Computer simulations are performed for the material parameters of AMLC-0010 and *d*/*p* = 1.5, fixed boundary conditions for the north-pole far-field preimage and U = 4.0 V.
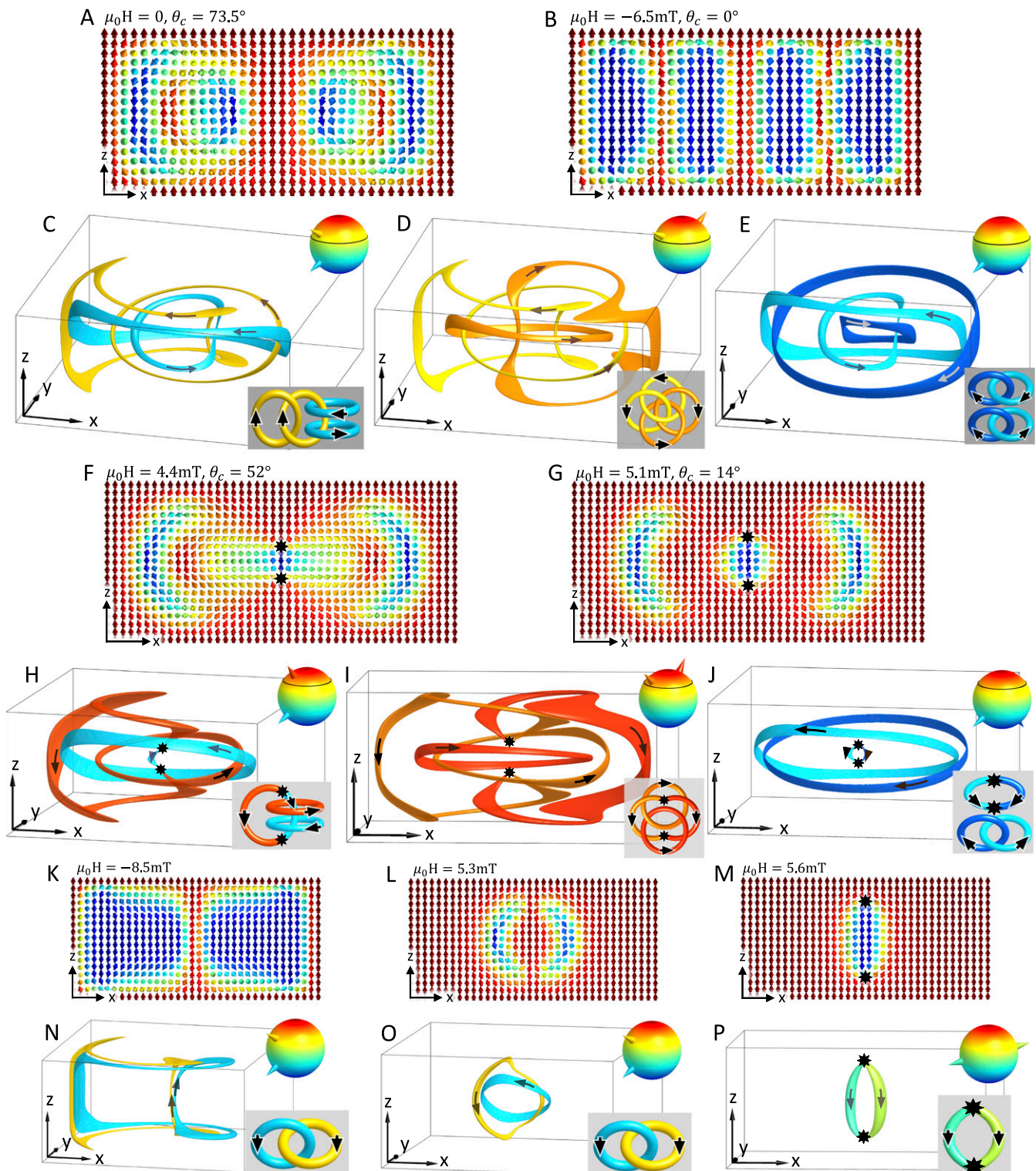
Fig. S4. Details of field-controlled structures and preimages of solitons shown in Fig. 7. (*A*, *B*, *F*, *G*, and *K–M*) Computer-simulated cross-sections in the plane parallel to **M₀** of the solitons stabilized at different applied fields. The strength of applied field $\mu_0 H$ and θ_c (if present) are indicated in the top left. Note that the field configurations of these solitons are all axially symmetric. (*C*, *D*, *E*, *H–J*, and *N–P*) Computer-reconstructed 3D preimages in $\mathbb{R}^3$ of points on $\mathbb{S}^2$ shown as cones in respective *Upper Right Insets*. The simplified schematics of the linking of preimages are shown in *Lower Right Insets*. In *A* and *B*, the $Q = 0$ solitons with complex linking of preimages are stabilized at $\mu_0 H = 0$ and $\mu_0 H = -6.5$ mT with $\theta_c = 73.5°$ and $\theta_c = 0°$, respectively. The preimages reconstructed in *C–E* correspond to the soliton pictured in *A*, for which the individual preimages form a Hopf link (2_1^2) in the case of $\mathbb{S}^2$ point at $\theta < \theta_c$ and two separate unlinked loops (0_1^2) for $\mathbb{S}^2$ points at $\theta > \theta_c$. For all combinations of preimages of distinct points on $\mathbb{S}^2$, the total linking number is 0, even though the behavior of individual preimages is characterized by two subspaces on $\mathbb{S}^2$. The θ_c boundary lines are shown as black circles on $\mathbb{S}^2$ in corresponding *Insets*. In *F* and *G*, the so-called "3π torons" with 3π twist from the central axis to periphery (4) are stabilized at $\mu_0 H = 4.4$ mT and $\mu_0 H = 5.1$ mT, with the subspace boundary lines at $\theta_c = 52°$ and $\theta_c = 14°$, respectively. The two regions of discontinuity in each field configuration are the hyperbolic point defects marked as filled black stars, at which some of the preimages terminate and **M(r)** is discontinuous. Each preimage in *H–J* of the 3π-toron in *F* is composed of a single closed loop and a half-loop band terminating on the singular point defects. They are linked depending on the subspace of $\mathbb{S}^2$ that they correspond to. In *K* and *L*, elementary hopfions with $Q = -1$ are stabilized at $\mu_0 H = -8.5$ mT and $\mu_0 H = 5.3$ mT, respectively. The preimages of two distinct points shown in *N* and *O* form Hopf links with linking numbers of -1. In *M*, an elementary toron (4, 25) is stabilized at $\mu_0 H = 5.6$ mT, and preimages form bands terminating on the two hyperbolic point defects, as shown in *P*. Computer simulations were performed for the material parameters of ZLI-2806, $d/p = 2.7$, and fixed boundary conditions along **M₀**, both at the confining substrates and in the far-field exterior of the localized structures.

Table S1. Linking graph diagrams and Hopf indices Q of the studied topological solitons

Preimages of solitons	Linking diagrams for vector fields with the ground-state manifold $\mathbb{S}^2$			Linking diagrams for the nonpolar director fields with the ground-state manifold $\mathbb{S}^2/\mathbb{Z}_2$			Q as a linking number	Q obtained numerically using Eq. 1
0_1^2 (Fig. 3A)							-2	-1.99903
$0_1^2, 0_1$ (Fig. 3B)	Both $\theta < \theta_c$	Both $\theta > \theta_c$	One $\theta < \theta_c$ and one $\theta > \theta_c$	$\theta < \theta_c \quad \theta < \theta_c$	$\theta > \theta_c \quad \theta > \theta_c$	$\theta < \theta_c \quad \theta > \theta_c$	-2	-1.99690
0_1 (Fig. 3C)							-1	-0.99952
0_1^2 (Fig. 5A)							0	-4.85722×10^{-5}
$0_1^2, 0_1$ (Fig. 5B)	Both $\theta < \theta_c$	Both $\theta > \theta_c$	One $\theta < \theta_c$ and one $\theta > \theta_c$	$\theta < \theta_c \quad \theta < \theta_c$	$\theta > \theta_c \quad \theta > \theta_c$	$\theta < \theta_c \quad \theta > \theta_c$	0	-9.34055×10^{-4}
0_1 (Fig. 5C)							-1	-0.99960
$2_1^2, 0_1, 0_1^2$ (Fig. 6A)	Both points in I / One in I and one in II	Both points in II / One in II and one in III	Both points in III / One in I and one in III	I I / I II	II II / II III	III III / I III	-2	-1.99825
$2_1^2, 0_1^2$ (Fig. 7A)	Both $\theta < \theta_c$	Both $\theta > \theta_c$	One $\theta < \theta_c$ and one $\theta > \theta_c$	$\theta < \theta_c \quad \theta < \theta_c$	$\theta > \theta_c \quad \theta > \theta_c$	$\theta < \theta_c \quad \theta > \theta_c$	0	-1.70859×10^{-5}
0_1 (Fig. S4K)							-1	-0.99850
0_1 (Fig. S4L)							-1	-0.99906

In the diagrams for solitons in the vector fields, colored filled circles represent closed-loop preimages of two distinct points on $\mathbb{S}^2$, with the colors indicative of the points on $\mathbb{S}^2$. The red (black) lines indicate positive (negative) signs of linking between closed loops determined by circulations. The linking between closed loops that each belong to the same preimage are indicated by dashed lines and is not counted toward the linking number between distinct preimages. In the diagrams for solitons in the director fields, closed loops represented by filled circles that belong to the same preimage are grouped, with the corresponding subspace of the point on $\mathbb{S}^2$ indicated if boundary lines are present. The Q values determined as the preimage linking numbers and via numerical integration using Eq. 1 for vectorized n(r) and M(r) agree up to the numerical error.

Table S2. Material parameters

Nematic LC host	K_{11} (pN)	K_{22} (pN)	K_{33} (pN)	$\varepsilon_\parallel$	$\varepsilon_\perp$	$\Delta\varepsilon$	Δn	ξ ofCB-15(μm^{-1})	ξ of ZLI-811(μm^{-1})
AMLC-0010	17.2	7.5	17.9	3.4	7.1	−3.7	0.08	—	10.47
ZLI-2806	14.9	7.9	15.4	3.3	8.1	−4.8	0.04	5.9	—

The table lists elastic and dielectric constants, optical and dielectric anisotropy values of the used nematic LC hosts, and helical twisting power ξ of the used chiral additives when doped into these nematic hosts. These experimentally determined (4, 8, 25, 26) material parameters were utilized in numerical modeling.
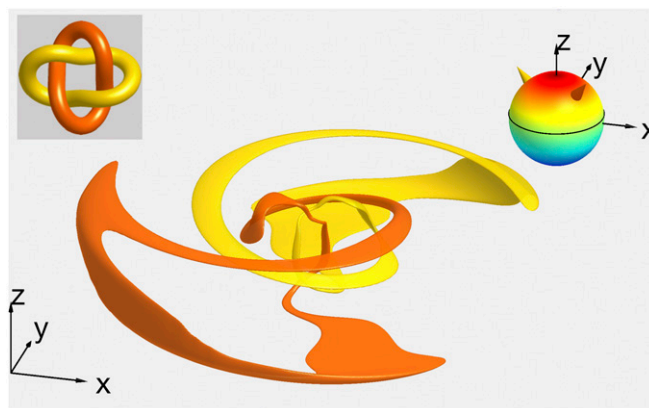
Movie S1.   Individual preimages and linking of preimages of pairs of points within different subspaces of $\mathbb{S}^2$ for a $Q = -2$ complex Hopf soliton depicted in Fig. 3B. *Right Inset* shows the $\mathbb{S}^2$ order parameter space with the circle-like boundary line at θ_c and the points corresponding to preimages shown using cones of corresponding colors. *Left Inset* shows the simplified schematics of preimages.
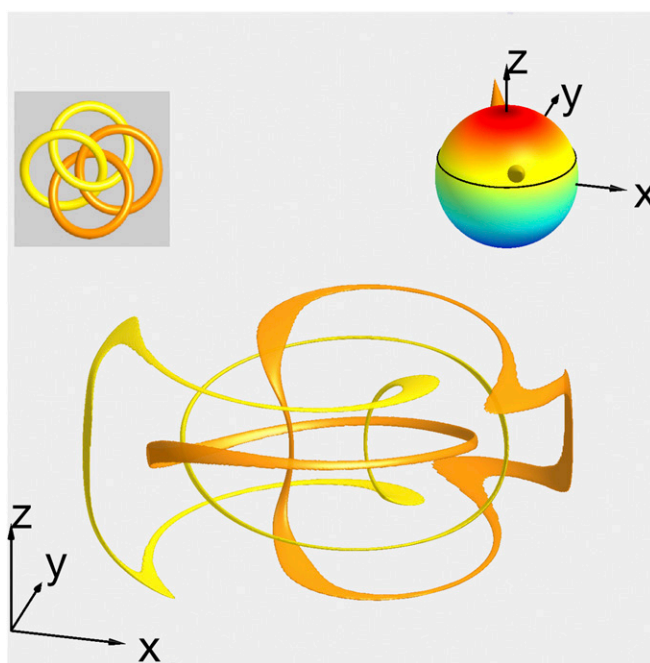
[Movie S1](#)
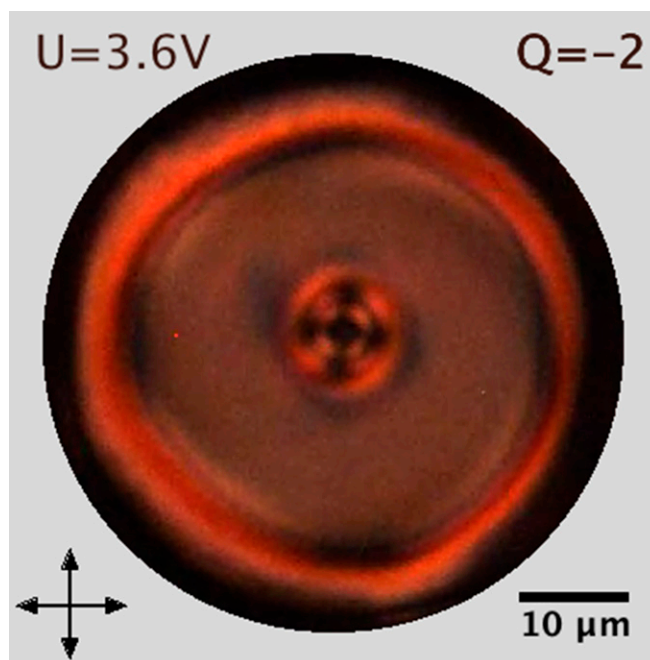
Movie S2.   Experimental POM video shows a $Q = -2$ soliton first transforming while retaining $Q = -2$ and then discontinuously transitioning into a $Q = -1$ soliton. The black double arrows show the crossed polarizer and analyzer. The applied voltage is indicated in the upper left corner. The values of Q are shown in the upper right corner.

[Movie S2](#)

Movie S3. Individual preimages and linking of preimages of pairs of points in different subspaces on $\mathbb{S}^2$ for a $Q = 0$ composite soliton depicted in Fig. 5*B*. *Right Inset* shows the $\mathbb{S}^2$ order parameter space with the circle-like boundary line at θ_c and the points corresponding to preimages shown using cones of corresponding colors. *Left Inset* shows the simplified schematics of preimages.

Movie S3

Movie S4. Individual preimages and linking of preimages of pairs of points in different subspaces on $\mathbb{S}^2$ for a $Q = 0$ composite soliton depicted in Fig. 7*A*. *Right Inset* shows the $\mathbb{S}^2$ order parameter space with the circle-like boundary line at θ_c and the points corresponding to preimages shown using cones of corresponding colors. *Left Inset* shows the simplified schematics of preimages.

Movie S4